J. Fluid Mech. (2010), *vol.* 662, *pp.* 66–90.
doi:10.1017/S0022112010003137

Dipolophoresis in large-scale suspensions of ideally polarizable spheres

JAE SUNG PARK AND DAVID SAINTILLAN†

Department of Mechanical Science and Engineering, University of Illinois at Urbana-Champaign, Urbana, IL 61801, USA

(Received 26 February 2010; revised 26 May 2010; accepted 1 June 2010; first published online 17 September 2010)

The nonlinear dynamics of uncharged ideally polarizable spheres freely suspended in a viscous electrolyte in a uniform electric field are analysed using theory and numerical simulations. When a sphere polarizes under the action of the field, it acquires a non-uniform surface charge, which results in an electro-osmotic flow near its surface that scales quadratically with the applied field magnitude. While this so-called induced-charge electrophoresis yields no net motion in the case of a single sphere, it can drive relative motions by symmetry breaking when several particles are present. In addition, Maxwell stresses in the fluid also result in non-zero dielectrophoretic forces, which also cause particle motions. The combination of these two nonlinear electrokinetic effects, termed dipolophoresis, is analysed in detail by using numerical simulations. An efficient simulation method based on our previous analysis of pair interactions is presented and accounts for both far-field and near-field electric and hydrodynamic interactions in the thin-Debye-layer limit, as well as steric interactions using a novel contact algorithm. Simulation results in large-scale suspensions with periodic boundary conditions are presented. While the dynamics under dielectrophoresis alone are shown to be characterized by particle chaining along the field direction, in agreement with previous investigations, chaining is not found to occur under dipolophoresis, which instead causes transient particle pairings and results in a non-uniform microstructure with large number of density fluctuations, as we demonstrate by calculating pair distribution functions and particle occupancy statistics. Dipolophoresis is also found to result in significant hydrodynamic dispersion and velocity fluctuations, and the dependence of these two effects on suspension volume fraction is investigated.

Key words: electrokinetics, particle/fluid flows, Stokesian dynamics, suspensions

1. Introduction

Electrokinetic flows, which result from the interaction of ionic screening clouds and applied electric fields in viscous electrolytes, provide an efficient and low-cost means for manipulating fluid and particles at small scales. They play a major role in micro- and nanofluidics (Squires & Quake 2005), colloidal and interfacial science (Russel, Saville & Schowalter 1989; Hiemenz & Rajagopalan 1997), particle and macromolecular separations (Viovy 2000), among other fields. The classical setting for electrokinetic flows consists of a rigid surface with a fixed charge density in

† Email address for correspondence: dstn@illinois.edu

contact with an electrolyte (or ionic solution). The surface charge repels co-ions and attracts counter-ions in the liquid. The latter migrate and accumulate near the surface, resulting in the formation of a diffuse charge cloud or Debye layer of characteristic thickness λ_D. As an external electric field $\boldsymbol{E}_0$ is applied, an effective body force is exerted on the ions near the surface. Next to a fixed surface (e.g. a boundary in a microfluidic device), this body force drives an electro-osmotic flow; in the case of a freely suspended particle in a quiescent liquid, it results in particle migration by electrophoresis. In both cases, fluid and particle velocities are found to scale linearly with the applied field.

In the thin-Debye-layer limit, i.e. when the Debye thickness λ_D is much less than the geometric length scale of interest, these flows can be captured via an effective slip velocity at the outer edge of the Debye layer, given by the Helmholtz–Smoluchowski equation

$$\boldsymbol{u}_s = -\frac{\varepsilon\zeta}{\eta}\boldsymbol{E}_s, \tag{1.1}$$

where ε and η are the electric permittivity and dynamic viscosity of the electrolyte, respectively, ζ is the zeta potential or potential drop across the Debye layer and is a material property related to the surface charge, and $\boldsymbol{E}_s$ is the local value of the electric field near the surface. This slip velocity then enters the boundary condition in the Stokes equations for the resulting fluid flow, which can be solved to determine fluid and particle velocities. In the case of a freely suspended sphere with uniform surface charge undergoing electrophoresis, the particle linear velocity is classically obtained as $\boldsymbol{U} = (\varepsilon\zeta/\eta)\boldsymbol{E}_0$ (Smoluchowski 1903; Henry 1931).

An interesting consequence of the boundary condition (1.1), first noted by Morrison (1970), is that the flow generated by the slip velocity around a particle with uniform zeta potential is a potential flow, i.e. the fluid velocity is everywhere proportional to the local electric field. An interesting consequence of this observation is that the electrophoretic velocity of a particle does not depend on its shape (i.e. non-spherical particles migrate at the same velocity as spherical particles), and electrophoresis does not cause particles to rotate (Morrison 1970). The flow also remains irrotational when several particles with identical zeta potentials are present, and a consequence of this observation is that hydrodynamic interactions do not occur in suspensions undergoing linear electrophoresis: all the particles migrate at the same velocity as if they were isolated, irrespective of their separation and orientation in the electric field (Reed & Morrison 1975; Anderson 1985; Chen & Keh 1988; Patankar 2009), at least as long as the particles are suspended in an unbounded domain (Acrivos, Jeffrey & Saville 1990). As a result, relative motions do not occur. Therefore, particles cannot be separated by size, and hydrodynamic dispersion is negligible.

The assumptions for these results to hold, namely thin Debye layers, weak applied fields, zero polarizability and surface conduction, however, are quite stringent and are hardly all satisfied in most experiments. When some of them are relaxed, nonlinear effects may arise and cause relative motions. The study of induced-charge electrokinetic flows, which arise when particles (or surfaces) are polarizable and can acquire an additional induced charge when placed in an external field (e.g. Bazant & Squires 2004, 2010; Squires & Bazant 2004; Squires 2009), has been of recent interest. This induced charge generally results in the formation of a non-uniform zeta potential distribution, which, in turn, drives an induced-charge electro-osmotic flow near the surface. Because the surface charge itself (and corresponding induced zeta potential) is driven by the electric field, this induced-charge flow is

easily seen to scale quadratically with the applied field. In the case of suspended particles in an electrolyte, this phenomenon, first analysed in the Soviet and post-Soviet colloidal literature (e.g. Simonov & Dukhin 1973; Gamayunov, Murtsovkin & Dukhin 1986; Murtsovkin 1996), was recently termed induced-charge electrophoresis (ICEP) by Squires & Bazant (2004). For a single ideally polarizable spherical particle, the ICEP flow can be determined exactly, and is found not to result in particle motion. Symmetry breaking is required for motion to occur (Squires & Bazant 2006): non-spherical particles rotate under ICEP (Yariv 2005; Saintillan, Darve & Shaqfeh 2006*a*; Rose *et al.* 2007; Yossifon, Frankel & Miloh 2007), and particle translation can also arise as a result of lack of fore–aft symmetry (Squires & Bazant 2006), as well as interactions with boundaries (Zhao & Bau 2007; Abu Hamed & Yariv 2009; Yariv 2009) or with neighbouring particles (Dukhin 1986; Dukhin & Murtsovkin 1986; Gamayunov *et al.* 1986; Saintillan *et al.* 2006*a*; Saintillan 2008; Rose *et al.* 2009).

Because of the quadratic dependence of these induced-charge flows with the applied field, a self-consistent calculation of the resulting particle motions also requires accounting for the Maxwell stress tensor in the fluid

$$\boldsymbol{\Sigma}^m = \varepsilon\left(\boldsymbol{EE} - \tfrac{1}{2}E^2\boldsymbol{I}\right), \tag{1.2}$$

the magnitude of which is of order $O(\varepsilon E_0^2)$ as for the hydrodynamic stresses generated by ICEP. These stresses account for dielectrophoretic (DEP) forces and torques on the particles, which can also cause particle motion (Pohl 1978; Jones 1995; Wang, Wang & Gascoyne 1997). While the DEP force on an isolated sphere in a uniform electric field is zero, non-zero forces again occur when symmetries are broken, for instance when several particles are present in a suspension (Saintillan 2008). When DEP occurs alone (i.e. when ICEP is negligible, for instance, with non-polarizable particles), its effect in particle suspensions is to cause aggregation, typically in the form of chains aligned with the field direction (e.g. Füredi & Valentine 1962; Jones 1995). The combined effect of ICEP and DEP, a phenomenon sometimes referred to as dipolophoresis (DIP) (Shilov & Simonova 1981), however, is more subtle.

While the effects of DIP have been well characterized for a single isolated particle in an arbitrary external field (e.g. Simonova, Shilov & Shramko 2001; Miloh 2008*a*, *b*, 2009), the case of interacting particles has received less attention. Interactions between spherical particles under ICEP alone were first analysed by Dukhin and co-workers, who derived an asymptotic expression for the relative velocity of a pair of widely separated ideally polarizable spheres (Dukhin 1986; Dukhin & Murtsovkin 1986; Gamayunov *et al.* 1986). They found that ICEP results in particle attraction in the field direction, and repulsion in the transverse direction; their result, however, was not valid in the near field and did not include contributions from DEP. The effects of near-field interactions and of DEP were more recently considered by Saintillan (2008), who used the more accurate method of twin multipole expansions and boundary-integral calculations to determine the relative motion of two identical spheres at arbitrary separation distances. This study confirmed the dynamics predicted by Dukhin and co-workers, suggesting that DIP should result in transient particle pairings in large suspensions.

The dynamics in large-scale particle suspensions undergoing ICEP or DIP have received little attention until now. The case of suspensions of Brownian and non-Brownian rod-like particles was recently considered in a series of computational studies (Saintillan *et al.* 2006*a*; Saintillan, Shaqfeh & Darve 2006*b*; Hoffman & Shaqfeh 2009). These studies neglected dielectrophoresis and only included ICEP,

on the basis that DEP interactions are weaker for high-aspect-ratio particles. They confirmed the occurrence of frequent particle pairings as predicted from pair interaction models, resulting in non-uniform pair distribution functions and in hydrodynamic particle diffusion at long time even in non-colloidal suspensions. These findings were also confirmed in experiments by Rose *et al.* (2009), with good agreement with the numerical simulations.

In this paper, we use numerical simulations to investigate the dynamics in large-scale suspensions of ideally polarizable (e.g. conducting) spheres under dipolophoresis. A simulation method is developed in § 2 based on the analysis of pair interactions of Saintillan (2008), and includes both ICEP and DEP far-field and near-field interactions, as well as steric interactions (excluded volume). These interactions are calculated efficiently by using the smooth particle mesh Ewald (SPME) algorithm of Saintillan, Darve & Shaqfeh (2005), allowing the simulation of suspensions of many particles. Simulation results are reported in § 3, where the pairing dynamics, suspension microstructure, hydrodynamic diffusion and velocity fluctuations are all analysed in detail for a variety of volume fractions ranging from dilute to semidilute ($\phi \sim 0.1$–$15\,\%$). We conclude in § 4.

2. Theory and simulation method

2.1. *Governing equations*

We consider a collection of N neutrally buoyant spheres of radius a, freely suspended in a viscous electrolyte with viscosity η and electric permittivity ε. The spheres are assumed to be identical, ideally polarizable (as would be the case for metallic or conducting particles), and to carry no net charge. As a result, linear electrophoresis will not occur in an electric field, allowing us to isolate the effect of dipolophoresis. We denote by $\boldsymbol{x}_\alpha$ the position of the centre of sphere $\alpha = 1, \ldots, N$ with respect to a fixed origin, and by S_α the surface of sphere α defined by $|\boldsymbol{x} - \boldsymbol{x}_\alpha| = a$. As an external uniform electric field $\boldsymbol{E}_0$ is applied, interactions between the spheres will arise as a result of both DEP and ICEP and may lead to relative motions. Next, we summarize the governing equations for both effects.

Under the action of the external field, each sphere polarizes, resulting in the formation of a non-uniform surface charge distribution. This charge distribution then attracts counter-ions in the electrolyte, which migrate and accumulate near the polarized surface, resulting in the formation of a non-uniform Debye layer. This charging of the Debye layer occurs on a very fast time scale, of the order of $\tau_c = \lambda_D a/D$, where λ_D is the Debye screening length and D is the characteristic diffusivity of the ions in solution (Squires & Bazant 2004). In a typical experiment ($\lambda_D \sim 10\,\text{nm}$, $a \sim 1\,\mu\text{m}$, $D \sim 10^{-5}\,\text{cm}^2\,\text{s}^{-1}$), the charging time τ_c is of the order of $10^{-5}\,\text{s}$. On time scales much larger than τ_c, the ionic cloud, therefore, effectively screens the induced non-uniform surface charge, in such a way that the particle and its charge cloud behave like an insulator. In the thin-Debye-layer limit of interest here ($\lambda_D \ll a$), the electric potential in the electroneutral bulk domain exterior to the charge clouds surrounding all the particles is, therefore, governed by Laplace's equation,

$$\nabla^2 \phi = 0, \tag{2.1}$$

subject to an effective no-flux boundary condition on the surface of the particles,

$$\hat{\boldsymbol{n}}_\alpha \cdot \nabla \phi = 0 \quad \text{as} \quad \boldsymbol{x} \in S_\alpha, \tag{2.2}$$

where $\hat{\boldsymbol{n}}_\alpha$ is the outward unit normal on the surface of sphere α. Rigorously, (2.2) applies at the outer edge of the charge clouds, which effectively coincides with the particle surfaces in the thin-Debye-layer limit. Finally, the electric potential is driven by the far-field condition

$$\nabla\phi \to -\boldsymbol{E}_0 \quad \text{as} \quad |\boldsymbol{x}| \to \infty. \tag{2.3}$$

The solution of (2.1)–(2.3) can generally be obtained using boundary-integral methods (Zinchenko 1994) or asymptotic methods (Jeffrey 1973).

Having determined the electric potential ϕ in the electrolyte, the electric field is easily obtained as $\boldsymbol{E} = -\nabla\phi$. Because of the presence of the particles, this field is non-uniform and will yield a non-zero Maxwell stress tensor $\boldsymbol{\Sigma}^m$, as defined in (1.2). This electrostatic stress tensor is responsible for the DEP forces and torques on the particles (Wang *et al.* 1997), which are obtained for particle α as

$$\boldsymbol{F}_\alpha = \int_{S_\alpha} (\boldsymbol{\Sigma}^m \cdot \hat{\boldsymbol{n}}_\alpha)\, \mathrm{d}S_\alpha, \tag{2.4}$$

$$\boldsymbol{T}_\alpha = \int_{S_\alpha} (\boldsymbol{x} - \boldsymbol{x}_\alpha) \times (\boldsymbol{\Sigma}^m \cdot \hat{\boldsymbol{n}}_\alpha)\, \mathrm{d}S_\alpha. \tag{2.5}$$

For a spherical particle subject to the boundary condition of (2.2), the dielectrophoretic torque $\boldsymbol{T}_\alpha$ is easily seen to be zero (Saintillan 2008). However, non-zero dielectrophoretic forces can be expected to arise by symmetry breaking even in a uniform external electric field as soon as several particles are present.

In addition to yielding DEP forces, the electric field also causes the motion of the counter-ions inside the double layers, driving a steady fluid flow near the particle surfaces. In the thin-Debye-layer limit, this induced-charge electro-osmotic flow can be captured by an effective slip velocity $\boldsymbol{u}_s$ on the surface of the spheres, which is modelled using the standard Helmholtz–Smoluchowski equation

$$\boldsymbol{u}_s^\alpha(\boldsymbol{x}) = -\frac{\varepsilon\zeta_\alpha(\boldsymbol{x})}{\eta}\boldsymbol{E}(\boldsymbol{x}) \quad \text{as} \quad \boldsymbol{x} \in S_\alpha, \tag{2.6}$$

where $\zeta_\alpha(\boldsymbol{x})$ now denotes the induced zeta potential corresponding to the induced surface charge resulting from polarization, and is obtained in terms of the electric potential drop across the charge cloud surrounding the particle of interest:

$$\zeta_\alpha(\boldsymbol{x}) = \phi_0^\alpha - \phi(\boldsymbol{x}) \quad \text{as} \quad \boldsymbol{x} \in S_\alpha. \tag{2.7}$$

For small zeta potentials ($\zeta_\alpha \ll kT/e$ where kT is the thermal energy and e is the ionic charge), ϕ_0^α is determined to enforce the neutrality condition on sphere α:

$$\int_{S_\alpha} \zeta_\alpha(\boldsymbol{x})\, \mathrm{d}S_\alpha = 0. \tag{2.8}$$

To determine the fluid velocity $\boldsymbol{u}$, particle translational velocities $\boldsymbol{U}_\alpha$ and angular velocities $\boldsymbol{\Omega}_\alpha$ resulting from both DEP and ICEP, the steady Stokes equations must be solved:

$$\eta\nabla^2\boldsymbol{u} = \nabla p, \quad \nabla \cdot \boldsymbol{u} = 0, \tag{2.9}$$

subject to a slip boundary condition on the particle surfaces,

$$\boldsymbol{u}(\boldsymbol{x}) = \boldsymbol{u}_s^\alpha(\boldsymbol{x}) + \boldsymbol{U}_\alpha + \boldsymbol{\Omega}_\alpha \times (\boldsymbol{x} - \boldsymbol{x}_\alpha) \quad \text{as} \quad \boldsymbol{x} \in S_\alpha, \tag{2.10}$$

and to a homogeneous boundary condition far away from the particles, $\boldsymbol{u}(\boldsymbol{x}) \to \boldsymbol{0}$ as $|\boldsymbol{x}| \to \infty$. In (2.10), the slip velocity $\boldsymbol{u}_s^\alpha(\boldsymbol{x})$ is obtained from the

Helmholtz–Smoluchowski equation (2.6). In addition, we impose a force and torque balance on each particle to close the system of equations,

$$\int_{S_\alpha} (\boldsymbol{\Sigma}^h \cdot \hat{\boldsymbol{n}}_\alpha)\, \mathrm{d}S_\alpha + \boldsymbol{F}_\alpha = \boldsymbol{0}, \tag{2.11}$$

$$\int_{S_\alpha} (\boldsymbol{x} - \boldsymbol{x}_\alpha) \times (\boldsymbol{\Sigma}^h \cdot \hat{\boldsymbol{n}}_\alpha)\, \mathrm{d}S_\alpha = \boldsymbol{0}, \tag{2.12}$$

where $\boldsymbol{\Sigma}^h = -p\boldsymbol{I} + \eta(\nabla\boldsymbol{u} + \nabla\boldsymbol{u}^T)$ is the hydrodynamic stress tensor in the fluid, and $\boldsymbol{F}_\alpha$ is the dielectrophoretic force on particle α given by (2.4). Note that particle and fluid motions arise from two different forcing terms: the slip velocity $\boldsymbol{u}_s^\alpha$ on the particle surfaces, corresponding to ICEP; and the force $\boldsymbol{F}_\alpha$ on the particles, corresponding to DEP. Owing to the linearity of the Stokes equations, both types of motions can be solved for separately and superimposed. Solutions of (2.9)–(2.12) can again be obtained using boundary-integral methods (Pozrikidis 1992; Saintillan 2008) or asymptotic methods (Jeffrey & Onishi 1984; Kim & Karrila 1991; Saintillan 2008).

2.2. *Pair interactions*

The case of two identical spheres in an unbounded domain was analysed in detail in a previous paper (Saintillan 2008), and is briefly summarized here. Based on symmetries, it is easily shown that the total force on and translational velocity of the particle pair is zero, and that both spheres rotate at the same angular velocity:

$$\boldsymbol{F}_1 = -\boldsymbol{F}_2, \quad \boldsymbol{U}_1 = -\boldsymbol{U}_2, \quad \boldsymbol{\Omega}_1 = \boldsymbol{\Omega}_2. \tag{2.13}$$

Furthermore, $\boldsymbol{F}_1$, $\boldsymbol{U}_1$ and $\boldsymbol{\Omega}_1$ can be expressed in tensorial form as

$$\boldsymbol{F}_1 = 4\pi\varepsilon a^2\, \boldsymbol{\mathsf{F}} : \boldsymbol{E}_0\boldsymbol{E}_0, \tag{2.14}$$

$$\boldsymbol{U}_1 = (\varepsilon a/\eta)\, \boldsymbol{\mathsf{M}} : \boldsymbol{E}_0\boldsymbol{E}_0, \tag{2.15}$$

$$\boldsymbol{\Omega}_1 = (\varepsilon/\eta)\, \boldsymbol{\mathsf{W}} : \boldsymbol{E}_0\boldsymbol{E}_0. \tag{2.16}$$

In (2.14)–(2.16), $\boldsymbol{\mathsf{F}}$ and $\boldsymbol{\mathsf{M}}$ are two third-order tensors and $\boldsymbol{\mathsf{W}}$ is a third-order pseudo-tensor; all three are dimensionless and depend only on the geometric configuration of the two spheres. Note that $\boldsymbol{\mathsf{F}}$ arises as a result of DEP only, whereas $\boldsymbol{\mathsf{M}}$ and $\boldsymbol{\mathsf{W}}$ have contributions from both DEP and ICEP: $\boldsymbol{\mathsf{M}} = \boldsymbol{\mathsf{M}}^{dep} + \boldsymbol{\mathsf{M}}^{icep}$, $\boldsymbol{\mathsf{W}} = \boldsymbol{\mathsf{W}}^{dep} + \boldsymbol{\mathsf{W}}^{icep}$. Defining $\boldsymbol{R} = \boldsymbol{x}_2 - \boldsymbol{x}_1$ as the separation vector between the two spheres pointing from sphere 1 to sphere 2, their most general form, based on symmetry considerations, can be written in indicial notation as

$$F_{ijk} = f(\lambda)(\delta_{ij}\hat{R}_k + \delta_{ik}\hat{R}_j) + g(\lambda)\hat{R}_i\delta_{jk} + h(\lambda)\hat{R}_i\hat{R}_j\hat{R}_k, \tag{2.17}$$

$$M_{ijk} = l(\lambda)(\delta_{ij}\hat{R}_k + \delta_{ik}\hat{R}_j) + m(\lambda)\hat{R}_i\delta_{jk} + n(\lambda)\hat{R}_i\hat{R}_j\hat{R}_k, \tag{2.18}$$

$$W_{ijk} = w(\lambda)\epsilon_{ijl}\hat{R}_l\hat{R}_k, \tag{2.19}$$

where $\lambda = 2a/R \in [0, 1]$ and $\hat{\boldsymbol{R}} = \boldsymbol{R}/R$. In (2.17)–(2.19), ϵ_{ijl} is the Levi–Civita alternating tensor, and f, g, h, l, m, n and w are seven dimensionless scalar functions of λ. These functions were previously calculated by Saintillan (2008) using the method of reflections, which is valid for large separation distances (typically $\lambda \lesssim 0.6$), as well as with the more accurate method of twin multipole expansions and boundary-integral method. Here, we report only asymptotic results for the translational velocity valid to $O(\lambda^4)$, which will be the basis for modelling far-field interactions in multiparticle systems in § 2.3. In particular, the functions l, m and n corresponding to DEP- and

ICEP-induced motions were obtained as

$$l^{dep}(\lambda) = -\frac{1}{32}\lambda^4 + O(\lambda^5), \tag{2.20}$$

$$m^{dep}(\lambda) = -\frac{1}{32}\lambda^4 + O(\lambda^5), \tag{2.21}$$

$$n^{dep}(\lambda) = \frac{5}{32}\lambda^4 + O(\lambda^5) \tag{2.22}$$

and

$$l^{icep}(\lambda) = \frac{11}{64}\lambda^4 + O(\lambda^5), \tag{2.23}$$

$$m^{icep}(\lambda) = -\frac{9}{32}\lambda^2 + \frac{11}{64}\lambda^4 + O(\lambda^5), \tag{2.24}$$

$$n^{icep}(\lambda) = \frac{27}{32}\lambda^2 - \frac{55}{64}\lambda^4 + O(\lambda^5). \tag{2.25}$$

From the method of reflections (Saintillan 2008), it can be shown that multiple reflections modify only these tensors to order $O(\lambda^5)$ and higher, so that (2.20)–(2.25) correctly describe the leading-order DEP and ICEP interactions between the two widely separated particles even when other particles are present. The corresponding far-field tensors $\boldsymbol{M}_{FF}^{dep}$, and $\boldsymbol{M}_{FF}^{icep}$ can also be expressed in a more compact form in terms of fundamental solutions of the Stokes equations,

$$\boldsymbol{M}_{FF}^{dep} = \frac{1}{12}\,\boldsymbol{T}(\boldsymbol{R}/a) + O(\lambda^5), \tag{2.26}$$

$$\boldsymbol{M}_{FF}^{icep} = -\frac{9}{8}\,\boldsymbol{S}(\boldsymbol{R}/a) - \frac{11}{24}\,\boldsymbol{T}(\boldsymbol{R}/a) + O(\lambda^5), \tag{2.27}$$

where the two third-order tensors $\boldsymbol{S}$ and $\boldsymbol{T} = \nabla^2\boldsymbol{S}$ are the Green's functions for a Stokes dipole and for a potential quadrupole, respectively (Happel & Brenner 1965; Kim & Karrila 1991). In an unbounded domain, these are expressed in indicial notation as

$$S_{ijk}(\boldsymbol{R}) = -\frac{\delta_{ij}R_k}{R^3} + \frac{\delta_{ik}R_j}{R^3} + \frac{\delta_{jk}R_i}{R^3} - 3\frac{R_iR_jR_k}{R^5}, \tag{2.28}$$

$$T_{ijk}(\boldsymbol{R}) = -\frac{6}{R^5}(\delta_{ij}R_k + \delta_{ik}R_j + \delta_{jk}R_i) + 30\frac{R_iR_jR_k}{R^7}. \tag{2.29}$$

The pair dynamics resulting from these interactions were analysed by Saintillan (2008) and are summarized in figure 1, showing the radial and tangential components of the relative velocity $\boldsymbol{U} = \boldsymbol{U}_2 - \boldsymbol{U}_1 = -2\boldsymbol{U}_1$ between the two spheres as functions of the angle Θ between the axis of the two spheres and the direction of the external field ($\boldsymbol{E}_0 \cdot \hat{\boldsymbol{R}} = E_0\cos\Theta$). Specifically, both DEP and ICEP are attractive when the two particles are nearly aligned with the direction of the electric field, and repulsive when they are aligned in the transverse direction, as demonstrated by the sign of the radial relative velocity $U_r = \boldsymbol{U}\cdot\hat{\boldsymbol{R}}$ in figure 1(a). This transition from attraction to repulsion is illustrated more clearly in figure 2, where the critical angle Θ_c, at which the radial velocity changes sign, is plotted as a function of the separation distance between the two spheres. Both DEP and ICEP can, therefore, be expected to result in particle pairing in the field direction, and in particle separation in the transverse direction. The two types of motion are, however, significantly different, as demonstrated by

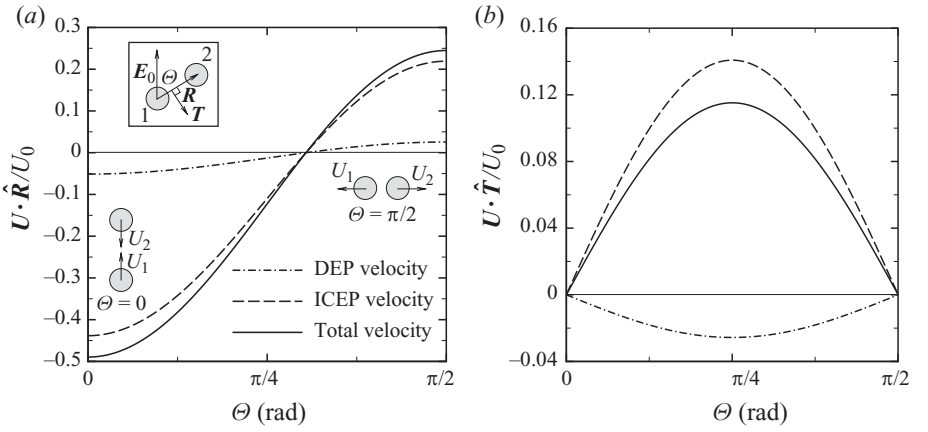

FIGURE 1. (*a*) Radial and (*b*) tangential components of the DEP, ICEP and total relative velocities between two spheres as functions of the angle Θ between the direction of the electric field $\boldsymbol{E}_0$ and the separation vector $\boldsymbol{R}$. Velocities have been scaled by $U_0 = (\varepsilon a/\eta)E_0^2$ and are evaluated at $R/a = 2.5$ (or $\lambda = 0.8$) based on the far-field expressions of (2.26)–(2.27).

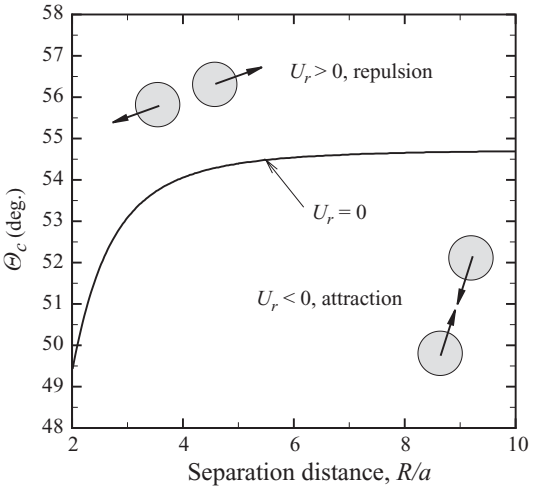

FIGURE 2. Critical value of the angle Θ for which the total radial velocity between two spheres is zero: $U_r = \boldsymbol{U} \cdot \hat{\boldsymbol{R}} = 0$, plotted as a function of the separation distance between the spheres. This critical angle separates configurations for which particle attraction ($U_r < 0$) and repulsion ($U_r > 0$) occur.

the tangential component of the relative velocity shown in figure 1(*b*): in the case of DEP, the aligned configuration (corresponding to $\Theta = 0$) is a stable equilibrium, whereas it is unstable for ICEP. In dipolophoresis, where both DEP and ICEP occur concurrently, ICEP is observed to dominate as a result of the slower $O(\lambda^2)$ decay of interactions, so that paired configurations are unstable. These observations will all be confirmed in simulations in § 3, where it is found that DEP alone causes particle chaining in the field direction, whereas DEP and ICEP together only result in transient particle pairings, by which two particles are attracted in the field direction, briefly pair up and separate in the transverse direction.

2.3. *Simulation method*

As described next, the analysis of pair interactions of § 2.2 can be used as the starting point for the simulation of large-scale suspensions of many interacting particles. Specifically, far-field interactions can be modelled using periodic analogues of (2.26)–(2.27), which are corrected in the near-field based on twin multipole expansions, as explained below. These interactions are also corrected for excluded volume as detailed in § 2.3.3.

2.3.1. *Electric and hydrodynamic interactions*

We consider a collection of N spherical particles in a periodic domain of linear dimensions $L_x \times L_y \times L_z$, and assume that the external electric field points in the z direction: $\boldsymbol{E}_0 = E_0\hat{\boldsymbol{z}}$. The motion of each particle results from DEP and ICEP interactions with the other $N-1$ particles in the domain, as well as with the periodic images of all N particles. Based on the analysis of § 2.2, the translational velocity $\dot{\boldsymbol{x}}_\alpha$ of a given particle α may be expressed as

$$\dot{\boldsymbol{x}}_\alpha = \frac{\varepsilon a E_0^2}{\eta} \sum_{\beta=1}^{N} \left[\tilde{\boldsymbol{M}}^{dep}(\boldsymbol{R}_{\alpha\beta}/a) + \tilde{\boldsymbol{M}}^{icep}(\boldsymbol{R}_{\alpha\beta}/a)\right] : \hat{\boldsymbol{z}}\hat{\boldsymbol{z}}, \quad \alpha = 1, \ldots, N, \tag{2.30}$$

where $\boldsymbol{R}_{\alpha\beta} = \boldsymbol{x}_\beta - \boldsymbol{x}_\alpha$ is the separation vector between particles α and β pointing from particle α to particle β, and where the two tensors $\tilde{\boldsymbol{M}}$ account for DEP and ICEP interactions, respectively. Specifically, for both DEP and ICEP, $\tilde{\boldsymbol{M}}$ is calculated as follows:

$$\tilde{\boldsymbol{M}}(\boldsymbol{R}_{\alpha\beta}/a) = \begin{cases} \boldsymbol{M}_P(\boldsymbol{R}_{\alpha\beta}/a) & \text{if } R_{\alpha\beta} \geqslant 4a, \\ \boldsymbol{M}_P(\boldsymbol{R}_{\alpha\beta}/a) - \boldsymbol{M}_{FF}(\boldsymbol{R}_{\alpha\beta}/a) + \boldsymbol{M}_{TM}(\boldsymbol{R}_{\alpha\beta}/a) & \text{if } R_{\alpha\beta} < 4a. \end{cases} \tag{2.31}$$

In (2.31), $\boldsymbol{M}_P$ denotes the periodic version of the far-field tensors $\boldsymbol{M}_{FF}^{dep}$ and $\boldsymbol{M}_{FF}^{icep}$ given in (2.26)–(2.27), which accounts for far-field interactions of particle α with particle β and all its periodic images; the method for calculating $\boldsymbol{M}_P$ is detailed in § 2.3.2. As discussed in § 2.2, these far-field tensors are asymptotically valid to order $O(R_{\alpha\beta}^{-4})$ for any pair of two particles α and β, and their use is, therefore, justified when particles are sufficiently far apart from each other, in this case when their separation distance is greater than $4a$. This ensures good accuracy, as demonstrated by Saintillan (2008). When particles come closer together ($R_{\alpha\beta} < 4a$), for instance during pairing events, the interaction tensors need to be corrected for the near-field interactions. This is achieved in (2.31) by replacing the far-field tensor $\boldsymbol{M}_{FF}$ for the direct interaction between particles α and β by a more accurate version $\boldsymbol{M}_{TM}$ calculated by Saintillan (2008) using the method of twin multipole expansions. This tensor is expressed in the form of (2.18), where the functions l, m and n are obtained by using cubic-spline interpolation from previously tabulated values (Saintillan 2008). While the twin-multipole expansion method cannot capture interactions when particles are almost touching, it still provides very accurate expressions down to separation distances of the order of $R_{\alpha\beta} \approx 2.05a$. At shorter separations, more accurate expressions could be obtained using lubrication theory. However, lubrication interactions between two spheres in DEP or ICEP have yet to be calculated (note that the lubrication theory for one sphere and a planar insulating wall under ICEP was recently worked out by Abu Hamed & Yariv 2009).

2.3.2. *The smooth particle mesh Ewald algorithm*

The calculation of the sums in (2.30) is a computationally expensive step with $O(N^2)$ operations if performed directly, and can become prohibitive for large values of N. To accelerate the calculation of these sums, we make use of an SPME algorithm, which is based on the Ewald summation formula of Hasimoto (1959) and on fast Fourier transforms, and reduces the cost of evaluating interactions to $O(N \log N)$. The SPME algorithm was previously developed by Saintillan *et al.* (2005) for point-force interactions in Stokes flow (Stokeslet interactions), and shares similarities with the accelerated Stokesian dynamics method of Sierou & Brady (2001). Here, the method of Saintillan *et al.* (2005) is used and adapted to model Stokes dipole and potential quadrupole interactions with periodic boundary conditions, as required by (2.26)–(2.27).

Specifically, we wish to evaluate sums of the form

$$\boldsymbol{u}_s(\boldsymbol{x}_\alpha) = \sum_{\beta=1}^{N} \boldsymbol{S}_P(\boldsymbol{x}_\beta - \boldsymbol{x}_\alpha) : \hat{\boldsymbol{z}}\hat{\boldsymbol{z}}, \tag{2.32}$$

$$\boldsymbol{u}_t(\boldsymbol{x}_\alpha) = \sum_{\beta=1}^{N} \boldsymbol{T}_P(\boldsymbol{x}_\beta - \boldsymbol{x}_\alpha) : \hat{\boldsymbol{z}}\hat{\boldsymbol{z}}, \tag{2.33}$$

for $\alpha = 1, \ldots, N$, where $\boldsymbol{S}_P$ and $\boldsymbol{T}_P$ denote the periodic versions of the Green's functions for a Stokes dipole and a potential quadrupole, respectively. Recalling that $\boldsymbol{S}_P = \nabla \boldsymbol{K}_P$ and $\boldsymbol{T}_P = \nabla^2 \boldsymbol{S}_P$, where $\boldsymbol{K}_P$ is the periodic Oseen–Burgers tensor (or Green's function for a periodic array of point forces in Stokes flow), and making use of the known Ewald summation formula for $\boldsymbol{K}_P$ (Hasimoto 1959; Saintillan *et al.* 2005), (2.32)–(2.33) can be recast into the following Ewald summations:

$$\boldsymbol{u}_s(\boldsymbol{x}_\alpha) = \sum_{\boldsymbol{p}} \sum_{\beta=1}^{N} \boldsymbol{A}_s(\xi, \boldsymbol{x}_\beta - \boldsymbol{x}_\alpha + \boldsymbol{p}) : \hat{\boldsymbol{z}}\hat{\boldsymbol{z}} + \sum_{\boldsymbol{k}\neq\boldsymbol{0}} \mathrm{e}^{-2\pi \mathrm{i}\boldsymbol{k}\cdot\boldsymbol{x}_\alpha} S(\boldsymbol{k}) \boldsymbol{B}_s(\xi, \boldsymbol{k}) : \hat{\boldsymbol{z}}\hat{\boldsymbol{z}}, \tag{2.34}$$

$$\boldsymbol{u}_t(\boldsymbol{x}_\alpha) = \sum_{\boldsymbol{p}} \sum_{\beta=1}^{N} \boldsymbol{A}_t(\xi, \boldsymbol{x}_\beta - \boldsymbol{x}_\alpha + \boldsymbol{p}) : \hat{\boldsymbol{z}}\hat{\boldsymbol{z}} + \sum_{\boldsymbol{k}\neq\boldsymbol{0}} \mathrm{e}^{-2\pi \mathrm{i}\boldsymbol{k}\cdot\boldsymbol{x}_\alpha} S(\boldsymbol{k}) \boldsymbol{B}_t(\xi, \boldsymbol{k}) : \hat{\boldsymbol{z}}\hat{\boldsymbol{z}}. \tag{2.35}$$

In (2.34)–(2.35), the first sums, or real sums, are over all the particle positions $\boldsymbol{x}_\beta$ and their periodic images (as denoted by the lattice vectors $\boldsymbol{p}$). The second sums, or Fourier sums, are over wavevectors $\boldsymbol{k}$ and involve the structure factor $S(\boldsymbol{k})$ of the suspension (Essmann *et al.* 1995):

$$S(\boldsymbol{k}) = \sum_{\beta=1}^{N} \exp(2\pi \mathrm{i}\boldsymbol{k} \cdot \boldsymbol{x}_\beta). \tag{2.36}$$

The parameter ξ in (2.34)–(2.35), called the Ewald coefficient, determines the relative importance of the real and Fourier sums; it is user-defined and is chosen to minimize the overall cost of the algorithm. The convolution kernels $\boldsymbol{A}_s$, $\boldsymbol{A}_t$, $\boldsymbol{B}_s$ and $\boldsymbol{B}_t$ are third-order tensors and can be obtained analytically in indicial notation as

$$A^s_{ijk}(\xi, \boldsymbol{x}) = -\pi\xi^{-3/2}\psi_{1/2}(\pi x^2/\xi)(4\delta_{ij}x_k - \delta_{ik}x_j - \delta_{jk}x_i) + 2\pi^2\xi^{-5/2}\psi_{3/2}(\pi x^2/\xi)(x^2\delta_{ij}x_k - x_i x_j x_k), \tag{2.37}$$

$$A^t_{ijk}(\xi,\boldsymbol{x}) = 2\pi^2\xi^{-5/2}\psi_{3/2}(\pi x^2/\xi)(28\delta_{ij}x_k - 7\delta_{ik}x_j - 7\delta_{jk}x_i) - 4\pi^3\xi^{-7/2}\psi_{5/2}(\pi x^2/\xi)(13x^2\delta_{ij}x_k - x^2\delta_{ik}x_j - x^2\delta_{jk}x_i - 9x_ix_jx_k) + 8\pi^4\xi^{-9/2}\psi_{7/2}(\pi x^2/\xi)(x^4\delta_{ij}x_k - x^2x_ix_jx_k) \quad (2.38)$$

and

$$B^s_{ijk}(\xi,\boldsymbol{k}) = -2\pi^2\mathrm{i}\,\xi^2\tau^{-1}\psi_1(\pi\xi k^2)(k^2\delta_{ij}k_k - k_ik_jk_k), \quad (2.39)$$

$$B^t_{ijk}(\xi,\boldsymbol{k}) = 8\pi^2\mathrm{i}\,\xi^2\tau^{-1}\psi_1(\pi\xi k^2)k^2(k^2\delta_{ij}k_k - k_ik_jk_k). \quad (2.40)$$

In (2.37)–(2.40), x^2 and k^2 stand for $|\boldsymbol{x}|^2$ and $|\boldsymbol{k}|^2$, respectively, $\tau = L_x \times L_y \times L_z$ is the volume of the periodic cell and ψ_ν denotes the incomplete Γ-function of order ν (Abramowitz & Stegun 1965). In particular,

$$\psi_1(x) = \frac{\exp(-x)}{x^2}(1+x), \quad \psi_{1/2}(x) = \frac{\exp(-x)}{x} + \frac{\sqrt{\pi}}{2x^{3/2}}\mathrm{erfc}(\sqrt{x}), \quad (2.41)$$

and the other functions are obtained using the recursion formula: $x\psi_\nu = \exp(-x) + \nu\psi_{\nu-1}$.

Note that all tensors $\boldsymbol{A}_s$, $\boldsymbol{A}_t$, $\boldsymbol{B}_s$ and $\boldsymbol{B}_t$ decay exponentially, so that the sums in (2.34)–(2.35) converge exponentially. In SPME, these are evaluated as follows (see Saintillan *et al.* 2005 for more details). The Ewald coefficient ξ is chosen so as to make all the terms in the real sums negligible beyond a fixed cutoff distance r_c: this allows truncation of these sums after a finite number of terms independent of the system size, resulting in an $O(N)$ cost for the evaluation of the real sums at all particle positions. For the second sums, or Fourier sums, the particle distribution is assigned to a Cartesian grid by B-spline interpolation (Essmann *et al.* 1995; Deserno & Holm 1997), and then transformed to Fourier space using the fast Fourier transform algorithm, yielding the structure factor $S(\boldsymbol{k})$. The structure factor is then multiplied by the convolution kernels $\boldsymbol{B}_s$ and $\boldsymbol{B}_t$. The inverse Fourier transform is applied, and interpolation is used to determine the values of the Fourier sums at the particle locations. The cost of the evaluation of the Fourier sums is limited by the fast Fourier transform algorithm, which scales as $O(K\log K)$ with the number K of grid points (or Fourier modes). This number is typically chosen to be proportional to the number of particles N, resulting in an $O(N\log N)$ overall cost for the evaluation of the velocities in (2.32)–(2.33), or equivalently for the evaluation of (2.30).

2.3.3. *Time marching and contact algorithm*

Having determined all the particle velocities $\dot{\boldsymbol{x}}_\alpha$ ($\alpha = 1,\ldots,N$) using (2.30) and the SPME algorithm, particle positions are advanced in time using a second-order Adams–Bashforth time-marching scheme, with an explicit Euler scheme for the first time step. A fixed time step Δt is used, and is chosen so as to ensure that particles only travel a fraction of the mean inter-particle distance during one integration step.

Because lubrication interactions are not included, and because of the use of finite time steps, hydrodynamic interactions are not sufficient to prevent particle overlap. In many simulation methods for particle dynamics at low Reynolds number, including Stokesian dynamics and its variants, particle overlap is avoided by introducing short-range repulsive forces which act when particles are close to contact (e.g. Nott & Brady 1994; Butler & Shaqfeh 2002). These short-range forces, while efficiently

preventing overlaps, are only an approximation to the actual hard-sphere potential between two solid particles, and may introduce spurious dynamics in the near-contact particle motions.

Here, we develop a contact algorithm, which also efficiently prevents overlaps without introducing any additional long-distance interactions. At each discrete time t_n, we denote $\Delta \boldsymbol{x}_\alpha^n = \boldsymbol{x}_\alpha^{n+1} - \boldsymbol{x}_\alpha^n$ as the displacement of particle α during the next time step if particle overlapping is ignored (i.e. if particle positions are simply advanced according to the velocities calculated in § 2.3.1). For each particle α, the set of particles β ($\beta = 1, \ldots, M$) that will overlap with α after performing this step can be determined, by checking whether $|\boldsymbol{x}_\beta^{n+1} - \boldsymbol{x}_\alpha^{n+1}| < 2a$. In most situations, $M = 1$ corresponding to a pair of overlapping particles, but in some cases M can be as large as 2 or 3, corresponding to a small cluster of overlapping particles. For each particle β with which overlap will occur, the fraction of Δt after which surface contact actually occurs, assuming that the particles move at a constant velocity during the time step, is calculated: this collision time, denoted by $\Delta t_c^{\alpha\beta}$, is obtained by solving the quadratic equation

$$\left|\boldsymbol{x}_\alpha^n - \boldsymbol{x}_\beta^n + \left(\Delta \boldsymbol{x}_\alpha^n - \Delta \boldsymbol{x}_\beta^n\right) \Delta t_c^{\alpha\beta} / \Delta t\right|^2 = (2a)^2. \tag{2.42}$$

Equation (2.42) has two solutions for $\Delta t_c^{\alpha\beta}$, but only one in the interval $[0, \Delta t]$: this solution is the relevant root and is chosen for $\Delta t_c^{\alpha\beta}$. Next, the particles $\beta = 1, \ldots, M$ are sorted by increasing values of $\Delta t_c^{\alpha\beta}$, i.e. such that $\Delta t_c^{\alpha 1} \leqslant \cdots \leqslant \Delta t_c^{\alpha\beta} \leqslant \cdots \leqslant \Delta t_c^{\alpha M}$. Finally, particle α is moved back to its original position $\boldsymbol{x}_\alpha^n$ and advanced according to the following expression:

$$\boldsymbol{x}_\alpha^{n+1} = \boldsymbol{x}_\alpha^n + \sum_{\beta=1}^{M} \hat{\boldsymbol{R}}_{\alpha\beta}^n \hat{\boldsymbol{R}}_{\alpha\beta}^n \cdot \left[\prod_{\gamma=1}^{\beta-1} (\boldsymbol{I} - \hat{\boldsymbol{R}}_{\alpha\gamma} \hat{\boldsymbol{R}}_{\alpha\gamma})\right] \cdot \Delta \boldsymbol{x}_\alpha^n \times \frac{\Delta t_c^{\alpha\beta}}{\Delta t} + \left[\prod_{\beta=1}^{M} (\boldsymbol{I} - \hat{\boldsymbol{R}}_{\alpha\beta} \hat{\boldsymbol{R}}_{\alpha\beta})\right] \cdot \Delta \boldsymbol{x}_\alpha^n, \tag{2.43}$$

where $\hat{\boldsymbol{R}}_{\alpha\beta}$ is the unit vector pointing from sphere α to sphere β. In the summation term corresponding to $\beta = 1$, the product over γ is simply replaced with the identity tensor. Equation (2.43) simply states that particle α is moved only a fraction $\Delta t_c^{\alpha\beta}/\Delta t$ of the full time step in the direction in which overlap would otherwise occur with particle β; the particle position, however, is still advanced a full step in the normal directions. This algorithm can be verified to prevent all overlaps (within roundoff errors) and to effectively model a hard-sphere potential without introducing unphysical long-distance interactions, as would be the case with a soft potential.

In the following discussion, governing equations and physical quantities are made dimensionless using the particle radius a as a characteristic length scale and the nonlinear velocity scale $\varepsilon a E_0^2/\eta$ with which both DEP and ICEP motions scale, as can be seen from (2.30).

3. Results and discussion

We now present results from large-scale simulations performed with the algorithm described above. Most of the data shown here were obtained in large-scale suspensions of 1000 to 3000 spheres, with the exception of figures 3–5, where only 100 particles were simulated for ease of visualization. We first describe results on the suspension microstructure under DEP alone and under DIP in § 3.1, and then analyse hydrodynamic diffusion and particle velocity statistics in §§ 3.2 and 3.3, respectively.

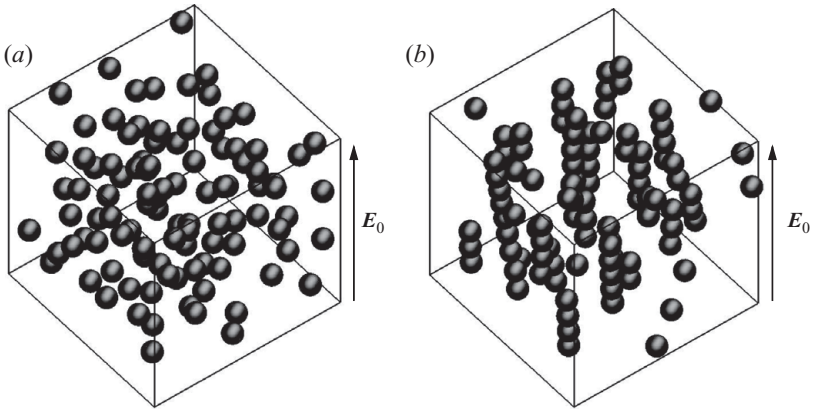

FIGURE 3. Particle distributions in a suspension of 100 spheres undergoing DEP alone in a periodic box of dimensions $L_x \times L_y \times L_z = 20^3$ (volume fraction $\phi = 5.24\,\%$) at times (*a*) $t = 0$ (random initial distribution), and (*b*) $t = 520$. As expected, DEP forces give rise to the formation of particle chains in the direction of the electric field. Also see the accompanying online movie available at journals.cambridge.org/flm.

3.1. *Particle dynamics and microstructure*

3.1.1. *Dynamics under dielectrophoresis*

Prior to presenting simulation results for particle dynamics under both DEP and ICEP in § 3.1.2, we first describe simulations obtained with dielectrophoresis alone (in the absence of induced-charge electrophoresis). This situation would be relevant to the case of non-polarizable particles, and may also qualitatively describe the case of dielectric particles for which ICEP is typically much weaker if not negligible (Squires & Bazant 2004). The anticipated effect in this case is the formation of particle chains as a consequence of the electric interactions between the induced dipoles on the particles: this particle chaining has been known for a long time and was previously characterized in both experimental and theoretical studies (e.g. Füredi & Valentine 1962; Pohl 1978; Jones 1995). This chaining is also clearly expected from the analysis of § 2.2 and based on figure 1, where we found that DEP interactions are attractive in the direction of the electric field, and that the aligned ('chained') configuration is a stable equilibrium in the case of two particles, unlike under ICEP interactions for which it is unstable. Figure 3 and the accompanying online movie show typical particle dynamics observed under DEP only. Starting from a random initial distribution (figure 3*a*), dielectrophoretic interactions cause particle configurations to rearrange, leading to the formation of long chains in the direction of the electric field (figure 3*b*). Eventually, chain growth becomes limited by the height of the simulation box and saturates. Also note that the motions resulting in this chain formation are quite slow (compared for instance to ICEP-induced motions, see § 3.1.2), and do not result in random particle motions or hydrodynamic diffusion: once the chains are formed the particles enter a frozen state where little to no motion occurs. Because particle chaining under DEP is a well-known phenomenon that has been characterized in the past, we now turn our focus more specifically on dipolophoresis, in which case the combined effects of DEP and ICEP are found to result in qualitatively different dynamics.

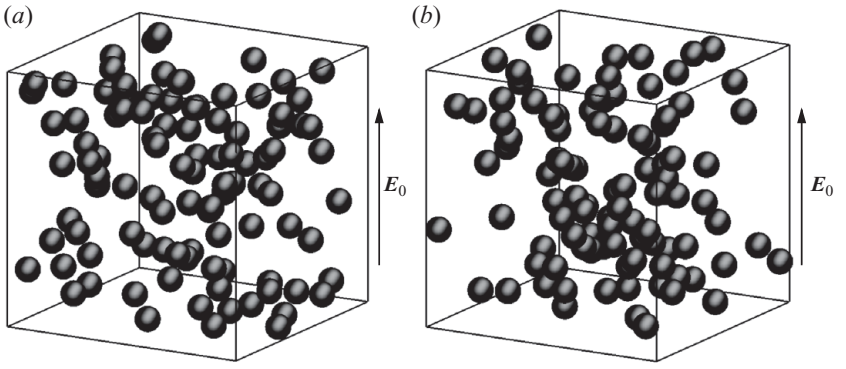

FIGURE 4. Particle distributions in a suspension of 100 spheres undergoing DIP (both DEP and ICEP) in a periodic box of dimensions $L_x \times L_y \times L_z = 20^3$ (volume fraction $\phi = 5.24\,\%$) at times (*a*) $t = 0$ (random initial distribution) and (*b*) $t = 400$. DIP is found to result in the formation of transient particle clusters, as seen in (*b*). Also see the accompanying online movie.

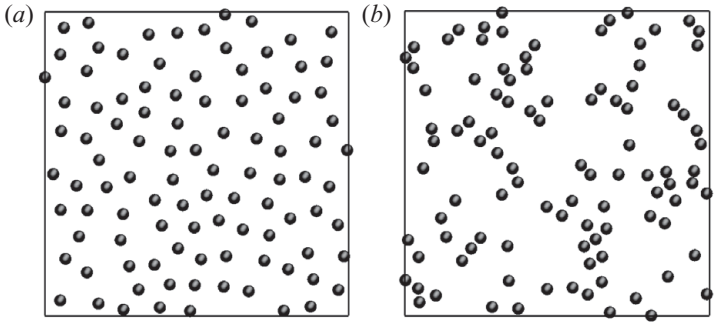

FIGURE 5. Two-dimensional particle distributions in a monolayer of 100 spheres undergoing DIP (both DEP and ICEP) in a periodic box of dimensions $L_x \times L_y \times L_z = 50 \times 3 \times 50$ (volume fraction $\phi = 5.59\,\%$) at times (*a*) $t = 0$ (random initial distribution) and (*b*) $t = 280$. The electric field points in the vertical direction. At $t = 280$, a non-uniform particle distribution is observed as a result of DIP interactions, with small clusters surrounded by clarified regions. Also see the accompanying online movie.

3.1.2. *Dynamics under dipolophoresis*

The dynamics in a suspension undergoing both DEP and ICEP are illustrated in figure 4 and the accompanying online movie. Starting from an initial random distribution, particles are found to undergo random chaotic motions as a result of DIP interactions: these motions constantly cause particle configurations to rearrange, but do not lead to the formation of chains as in the case of DEP interactions only (figure 3). Figure 4(*b*) also suggests that these particle configurations are not entirely random but exhibit clusters and depleted regions, which are transient and constantly break up and reform with time. These effects are more easily seen in figure 5 and the accompanying online movie, which show the dynamics in a two-dimensional particle monolayer. In this geometry, particle motions are seen to be characterized by frequent particle pairings, by which two particles are attracted in the direction of the electric field, pair up, and separate in the perpendicular direction. These frequent pairings in turn result in the formation of transient clusters as mentioned previously, and of clarified regions (figure 5*b*).

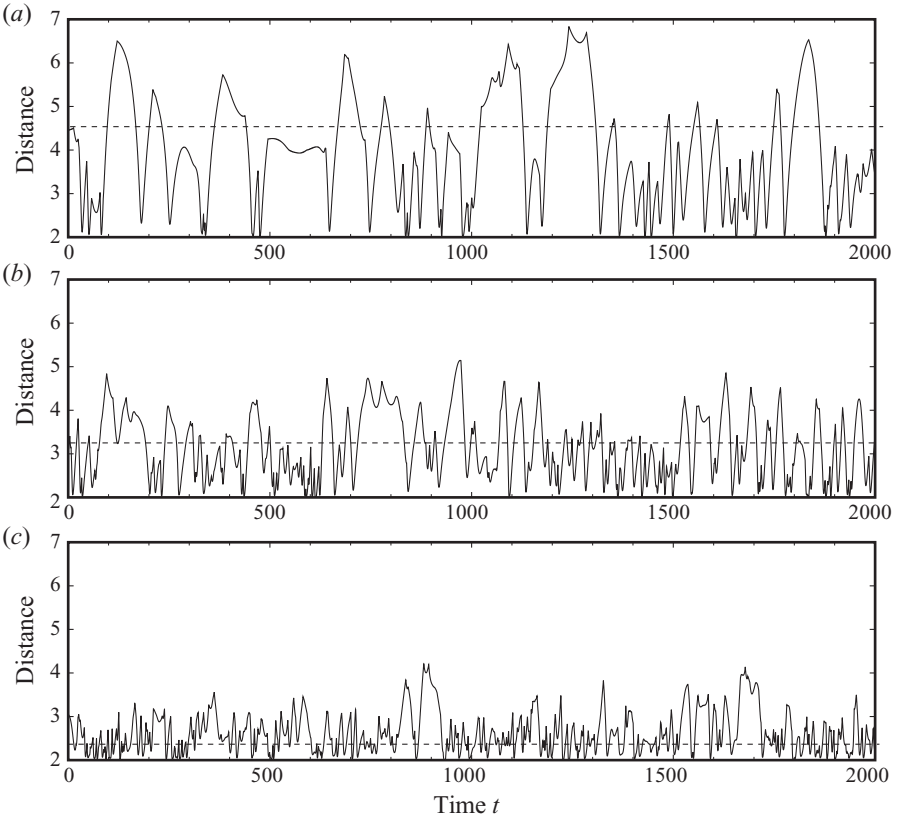

FIGURE 6. Separation distance from a test sphere to its nearest neighbour as a function of time in suspensions undergoing DIP, at volume fractions (*a*) $\phi = 0.98\,\%$, (*b*) $\phi = 3.02\,\%$ and (*c*) $\phi = 7.85\,\%$. In each case, the dotted line shows the mean inter-particle distance $a\phi^{-1/3}$. As volume fraction increases, fluctuations become more rapid indicating more frequent particle pairings.

The observed transient pairings are a direct consequence of the pair dynamics previously described by Saintillan (2008) and in § 2.2. DIP interactions indeed result in attraction in the direction of the electric field; the aligned configuration, however, is an unstable equilibrium when both DEP and ICEP occur, causing the particle pair to rotate and reorient in a direction perpendicular to the electric field. In this configuration, interactions become repulsive and cause the particles to separate. These pairing events are qualitatively similar to those previously predicted by Saintillan *et al.* (2006*a*) in suspensions of rod-like particles, which were also observed experimentally by Rose *et al.* (2009). Note, however, that in the case of high-aspect-ratio rod-like particles, DEP interactions can be neglected with respect to ICEP, owing to their scaling with the square of the inverse aspect ratio (Saintillan *et al.* 2006*a*).

These pairing events are further illustrated in figure 6, showing the time evolution of the distance from a test particle to its nearest neighbour over the course of three simulations at three distinct volume fractions ϕ. In each case, the minimum distance constantly fluctuates between a value of approximately two particle radii, corresponding to near contact, i.e. pairing, and a larger value of the order of the mean inter-particle distance $a\phi^{-1/3}$ for each given volume fraction. As volume fraction increases, the characteristic pairing frequency, or dominant frequency of

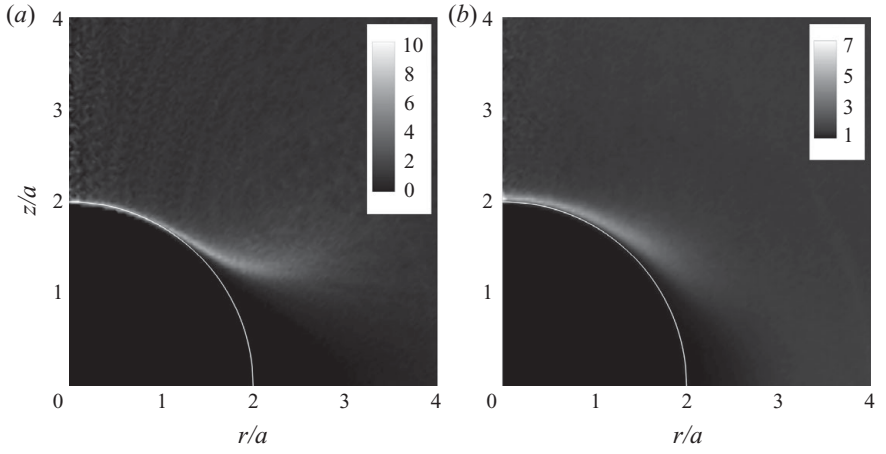

FIGURE 7. Pair distribution functions in suspensions of 1200 spheres undergoing DIP at volume fractions (*a*) $\phi = 1.5\,\%$ and (*b*) $\phi = 11.7\,\%$. The black region inside the white quarter circle corresponds to the region of excluded volume. Bright regions result from particle pairings in the direction of the electric field, while the depletion region along the horizontal axis is a consequence of the strong particle repulsion that occurs when two spheres are side by side.

the fluctuations in figure 6, is found to increase significantly, an effect that can be attributed to the lower mean separation distance which facilitates pairings, and to the stronger magnitude of DIP interactions in more concentrated suspensions.

The effects of pairings on the local microstructure of the suspensions may be investigated more quantitatively by calculating pair distribution functions $p(r, z)$ in cylindrical coordinates (with $r^2 = x^2 + y^2$), giving the probability of finding a particle at position (r, z), if a particle is located at the origin. Note that $p(r, z)$ is axisymmetrical and symmetrical with respect to the horizontal xy plane. Figure 7 shows two pair distribution functions at two different volume fractions, obtained from simulations. The black region inside the circle of radius $2a$ corresponds to excluded volume. The pair distributions are characterized by sharp peaks near the z-axis (pole of the particles), corresponding to a high probability of finding two particles aligned or nearly aligned in the direction of the electric field: these peaks are a direct consequence of the particle pairings described above. Conversely, the pair distributions also exhibit depletion regions near the equator, as demonstrated by the dark regions that extend radially about $z = 0$: these depletions are due to the repulsion that occurs when two particles are side by side. The two distributions at two different volume fractions are qualitatively very similar. Yet, it is found that the pairing region becomes less sharp as concentration increases; this is the likely consequence of the stronger hydrodynamic fluctuations occurring in concentrated suspensions, which result in stronger particle diffusion as discussed in § 3.2 and, therefore, somewhat hinder clear pairings. Note that the results of figure 7 are also consistent with previous theoretical, computational and experimental findings made on suspensions of rod-like particles (Saintillan *et al.* 2006*a*; Rose *et al.* 2009).

While the pair distribution functions of figure 7 characterize the effect of particle pairings on pair configurations, it is obvious from the distributions of figures 4 and 5 that DIP also results in a non-uniform and non-random microstructure on larger length scales, as demonstrated by the presence of particle clusters and clarified regions. To further investigate this feature, we present results for particle occupancy statistics,

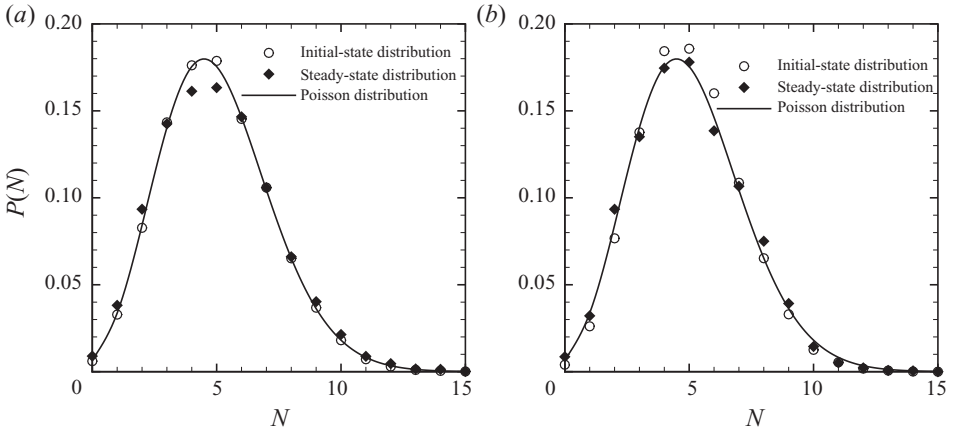

FIGURE 8. Particle occupancy distributions for $\langle N\rangle = 5$ in a suspension of volume fraction (*a*) $\phi = 0.37\,\%$ and (*b*) $\phi = 2.45\,\%$ undergoing DIP. The plots show the initial and steady-state distributions, as well as the Poisson distribution of (3.1). For both volume fractions, DIP interactions result in a broadening of the distributions, corresponding to an increase in number fluctuations as a result of particle clustering.

which characterize number-density fluctuations at arbitrary scales. Given a cubic interrogation cell of a given fixed volume V, we expect the mean number of particles inside the cell to be given by $\langle N\rangle = \phi V/V_p$ where ϕ is the volume fraction and $V_p = 4\pi a^3/3$ is the volume of one sphere. In practice, when such a cell is positioned arbitrarily inside the simulation box, it will contain a number N of particles that may differ from the expected value $\langle N\rangle$. The distribution $P(N)$ of this number of particles at a given $\langle N\rangle$ (or equivalently a given cell volume V) characterizes number-density fluctuations with respect to a perfectly homogeneous suspension. In a random suspension with particle positions obeying Poisson statistics, this distribution is known exactly and given by

$$P(N) = \frac{\langle N\rangle^N \mathrm{e}^{-\langle N\rangle}}{N!}. \tag{3.1}$$

Figure 8 shows the distribution $P(N)$ measured in the simulations for an interrogation cell containing $\langle N\rangle = 5$ particles on average. The two plots correspond to two volume fractions ϕ, and show occupancy statistics at $t = 0$ (initial random distribution) and at steady state under DIP; they also compare these distributions to the Poisson distribution of (3.1). At the lower volume fraction of $\phi = 0.37\,\%$ (figure 8*a*), the initial random distribution is well captured by a Poisson distribution as expected since excluded volume plays a negligible role in very dilute suspensions. However, at steady state, the distribution is found to depart from Poisson statistics: specifically the distribution is slightly broader, corresponding to larger number fluctuations on the scale of the interrogation box than in a random suspension, as expected from figures 4(*b*) and 5(*b*). At the higher volume fraction of $\phi = 2.45\,\%$ (figure 8*b*), similar trends are observed. In this case, the initial distribution departs slightly from Poisson statistics, which is a consequence of excluded volume, which prevents strong number fluctuations; however, under dipolophoresis, the distribution is found to broaden as well, as a result of particle clustering under DEP and ICEP interactions.

The departure from a random distribution as a result of interactions is also made more quantitative in figure 9, showing the standard deviation σ_N of the distributions

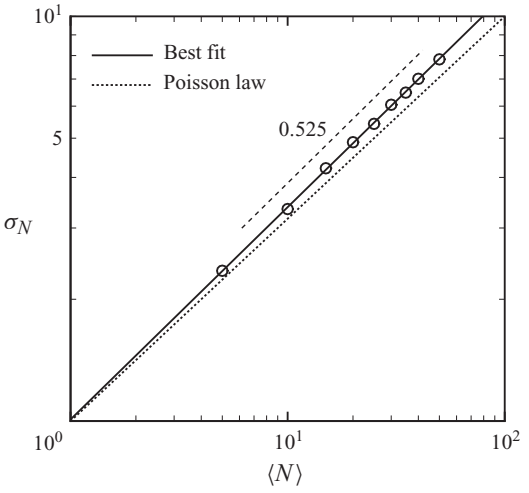

FIGURE 9. Standard deviation σ_N of the number of particles versus $\langle N \rangle$ in a suspension of volume fraction $\phi = 0.37\,\%$ under DIP. The standard deviation is well captured by a power law $\sigma_N \approx \langle N \rangle^{0.525}$ (solid line), which exceeds the Poisson law $\sigma_N = \langle N \rangle^{1/2}$ (dotted line).

$P(N)$ as a function of the expected mean $\langle N \rangle$, for a given volume fraction. The standard deviation is found to be well captured by a power law: $\sigma_N \approx \langle N \rangle^{0.525}$, which can be compared with the theoretical exponent of 1/2 for a Poisson distribution. This confirms that interactions under DIP result in larger number fluctuations than in random suspensions. The departures from the Poisson law, in both figures 8 and 9, however, remain quite weak, for instance compared with other suspension flows such as sedimentation, where strongly non-Poisson statistics have been reported in some cases (e.g. Lei, Ackerson & Tong 2001; Bergougnoux & Guazzelli 2009).

3.2. *Hydrodynamic dispersion*

Because of the frequent transient particle pairings that take place under DIP, particles in the suspension follow trajectories in space analogous to random walks. This is most easily seen in the online movies accompanying figures 4 and 5, and is also illustrated in figure 10, showing the trajectory of a sample particle in the two-dimensional simulation of figure 5. The trajectory is found to be random and chaotic; it exhibits smooth sections over which the particle meanders in space, separated by 'kinks' or sharp turns, which correspond to particle pairings. Over long times, such trajectories can be expected to result in an effective diffusive motion, the origin of which is not thermal but is hydrodynamic in nature. Hydrodynamic diffusion is common in suspensions of hydrodynamically interacting particles (e.g. Ham & Homsy 1988; Drazer *et al.* 2002; Pine *et al.* 2005), and has already been reported in suspensions of rod-like particles under ICEP (Saintillan *et al.* 2006*a*; Rose *et al.* 2009).

To quantify hydrodynamic diffusion under DIP, mean-square particle displacements versus time were calculated, and typical curves are shown in figure 11. As is usual for hydrodynamic diffusion, these curves exhibit an initial ballistic regime in which the mean-square displacements grow quadratically with time. After a few particle–particle interactions, particle motions start decorrelating in time, and a transition to a diffusive regime is observed, with a linear growth of the mean-square displacements. The transition between these two regimes is particularly clear in the log–log plot of figure 11(*b*). From these curves, an effective hydrodynamic diffusion tensor $\boldsymbol{D}$ can be

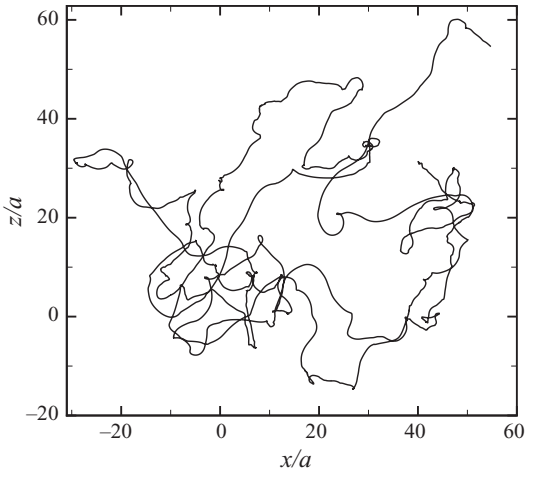

FIGURE 10. Typical particle trajectory in the simulation of figure 5. The particle is found to follow a random walk in space, with a trajectory exhibiting smooth sections separated by sharp turns corresponding to particle pairings.

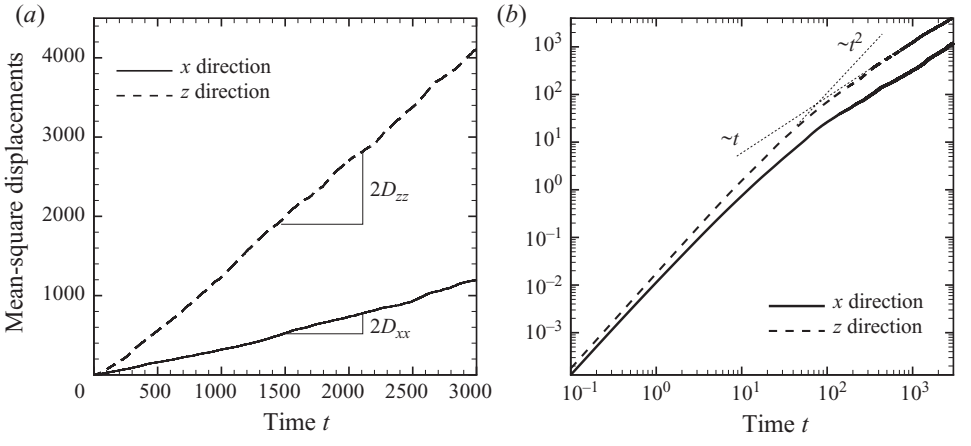

FIGURE 11. Mean-square displacement curves in the x and z directions as functions of time: (a) linear plot and (b) log–log plot. The log–log plot clearly shows an initial quadratic growth corresponding to ballistic motion, followed by a transition to a linear growth corresponding to hydrodynamic diffusion at long time. An effective hydrodynamic diffusion tensor can be inferred by $\langle(\boldsymbol{x}(t)-\boldsymbol{x}_0)(\boldsymbol{x}(t)-\boldsymbol{x}_0)\rangle \sim 2\boldsymbol{D}t$ as $t \to \infty$.

evaluated as

$$\boldsymbol{D} = \lim_{t\to\infty} \frac{1}{2}\frac{\mathrm{d}}{\mathrm{d}t}\langle(\boldsymbol{x}(t)-\boldsymbol{x}_0)(\boldsymbol{x}(t)-\boldsymbol{x}_0)\rangle, \tag{3.2}$$

where the angle brackets denote an ensemble average over all particles and several realizations of the same simulation. As expected from figure 11, the tensor $\boldsymbol{D}$ is anisotropic, with stronger diffusivities arising in the electric field direction than in the perpendicular directions: $D_{zz} > D_{xx} = D_{yy}$. The dependence of the diffusivities on suspension volume fraction is shown in figure 12, where the diffusivities are scaled by $\varepsilon a^2 E_0^2/\eta$. In the dilute to semidilute regime ($\phi \lesssim 5\,\%$), diffusivities are observed to grow with volume fraction, following a power law with exponent $\approx$0.25. Around

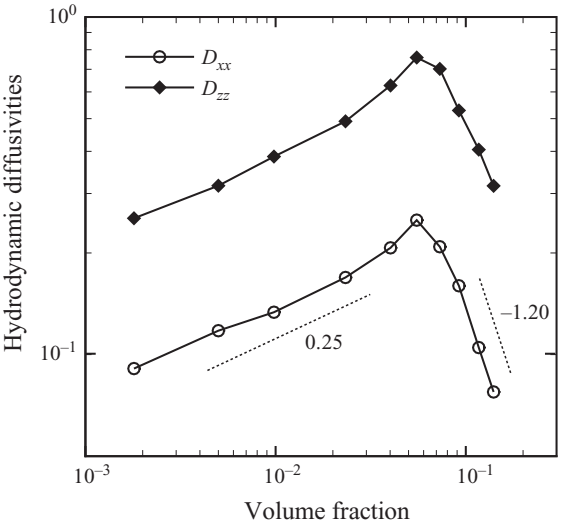

FIGURE 12. Hydrodynamic diffusivities in the directions parallel (z direction) and perpendicular (x direction) to the electric field as functions of volume fraction. The diffusivities were determined using mean-square displacement curves and (3.2).

$\phi \approx 5\,\%$, the diffusivities are found to reach a maximum, followed by a significant decrease at higher concentrations. The increase at low volume fractions is easily explained by the increase in the magnitude of particle–particle interactions with concentration. The subsequent decrease, however, is less easily explained, but may be a consequence of excluded volume interactions, which become significant and may hinder particle diffusion in concentrated suspensions. Over the entire range of volume fractions shown in figure 12, the ratio D_{zz}/D_{xx} of the diffusivities in the field direction and perpendicular directions is found to remain roughly constant and equal to ≈ 3.2. Note that all of these results are qualitatively consistent with the previous study of Saintillan *et al.* (2006*a*) on suspensions of rod-like particles under ICEP, where a similar diffusivity increase had been reported at low volume fractions.

3.3. *Velocity statistics*

We finish by reporting results on particle velocity statistics in the simulations. While DIP does not result in any net particle motions (in fact, the mean particle velocity over the whole suspension is exactly zero at all times), it does result in significant velocity fluctuations as a result of interactions. Typical velocity distributions in the z and x directions at two different volume fractions are shown in figure 13, where they are normalized to have an integral of 1, and are compared with Gaussian distributions with the same variance. Consistent with our findings on the diffusivities in § 3.2, we find that particle velocities are larger in the field direction than in the perpendicular directions, and that their typical magnitude increases with volume fraction. While the velocity distributions are well captured by Gaussian distributions at low-velocity magnitudes, they also exhibit broad tails that are clearly non-Gaussian, especially in the directions perpendicular to the electric field. This observation is not too surprising considering the simulations are not in thermal equilibrium.

Velocity fluctuations are quantified more precisely in figure 14, showing the standard deviation of the particle velocities in the field and perpendicular directions as functions of volume fraction. As expected, the fluctuations are found to be larger in the direction

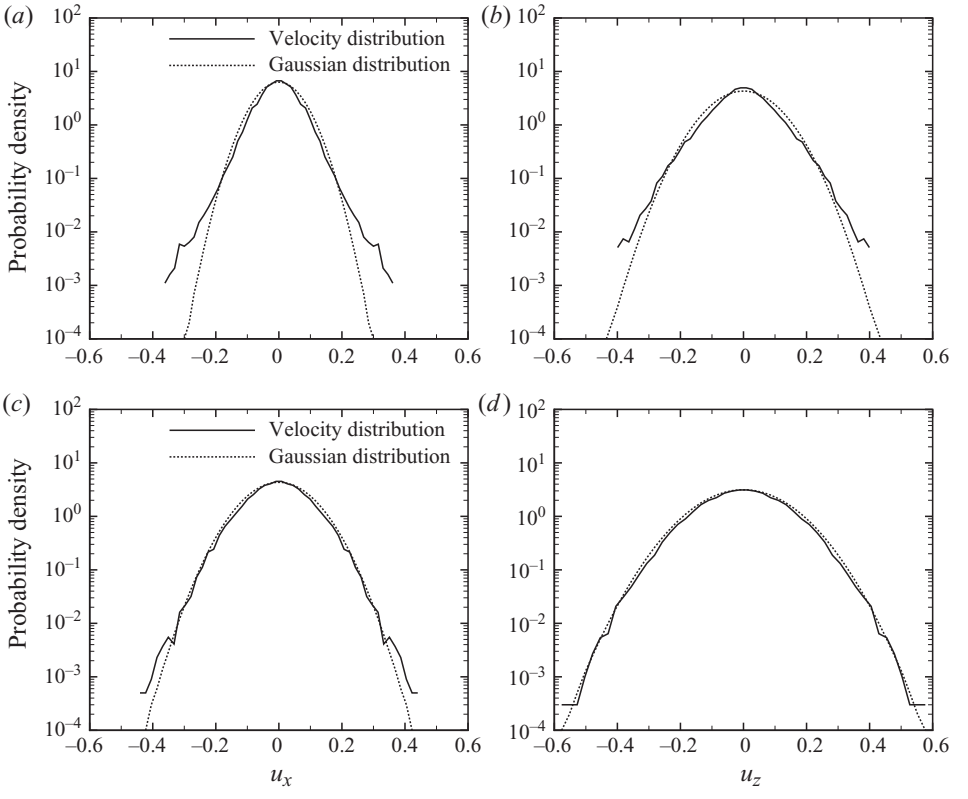

FIGURE 13. Particle velocity distributions in the x and z directions in suspensions undergoing DIP at a volume fraction of (*a*)–(*b*) $\phi = 1.5\,\%$, and (*c*)–(*d*) $\phi = 11.7\,\%$. The distributions are compared to Gaussian distributions with the same variance (dotted curves).

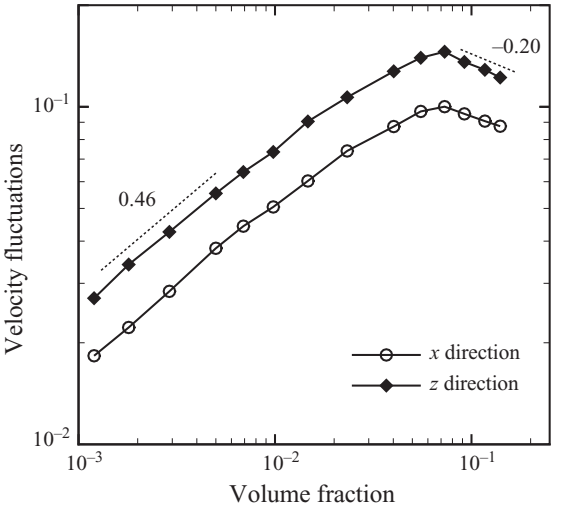

FIGURE 14. Standard deviations of particle velocities in the x and z directions as functions of volume fraction, in suspensions undergoing DIP.

of the electric field, and they are also found to grow with volume fraction in the dilute and semidilute regimes, according to an approximate power law with exponent ≈ 0.46. Beyond $\phi \approx 7\,\%$, they are found to saturate and eventually decay as ϕ increases further, in qualitative agreement with the behaviour observed on the particle diffusivities in figure 12.

4. Concluding remarks

We have presented a theoretical and computational study of particle motions resulting from electric and hydrodynamic interactions under dipolophoresis (or combination of dielectrophoresis and induced-charge electrophoresis) in suspensions of ideally polarizable spheres in a uniform externally applied electric field. Based on the previous study of Saintillan (2008), we first analysed pair interactions, which are found to be attractive in the direction of the electric field, but repulsive in the transverse direction. While DEP alone is found to result in particle chaining, with a stable equilibrium for two particles aligned in the direction of the electric field, this equilibrium becomes unstable when ICEP occurs as well, so that chaining should not occur. Instead, transient particle pairings are predicted, by which two particles are attracted in the direction of the field, pair up and separate in a perpendicular direction.

To confirm this analysis and investigate the effects of these interactions when many particles are present, an algorithm was developed to simulate large-scale sphere suspensions with periodic boundary conditions. The simulation method includes far-field and near-field DEP and ICEP interactions, steric effects via a contact algorithm, and is accelerated using an efficient SPME algorithm (Saintillan *et al.* 2005). Simulations in suspensions undergoing DEP alone (no induced-charge electrophoresis) exhibit the formation of long particle chains in the direction of the field, the growth of which is eventually limited by system size: this chaining is consistent with the analysis of pair interactions, and is a well-known phenomenon that has been characterized in the past. When ICEP occurs as well (i.e. under dipolophoresis), the chaining is found to disappear altogether, and is replaced by transient particle pairing events, in agreement with previous studies on rod suspensions (Saintillan *et al.* 2006*a*; Rose *et al.* 2009). These pairings are found to result in non-uniform pair distribution functions with peaks near the particle poles and depletions near the equators; in addition, they also lead to a non-uniform microstructure, with the formation of transient clusters and clarified regions, as demonstrated by the large number fluctuations measured in the simulations, which exceed those of a random suspension. In addition, these motions result in significant velocity fluctuations and in hydrodynamic diffusion at long time, both of which are found to become stronger with volume fraction in the dilute and semidilute regimes.

The interactions in this study are likely to play a role in all applications in which polarizable particles are placed in an external electric field, including in electrophoresis. They have often been overlooked in the past on the basis that they scale quadratically with the electric field strength, and therefore, should be negligible compared to electrophoretic motions in weak fields. However, the typical magnitude of DIP-induced motions is $O(\varepsilon a E_0^2/\eta)$, while electrophoretic motions scale with $O(\varepsilon\zeta E_0/\eta)$, where ζ is the native zeta potential of the particles: DIP should therefore become significant when $aE_0/\zeta \sim O(1)$. In a typical microfluidic experiment for which $a \sim$ 1–10 μm, $\zeta \sim 10$–100 mV, and $E_0 \sim 10$–$100\,\mathrm{V\,cm^{-1}}$, we expect $aE_0/\zeta \sim 0.01$–10, which suggests that DIP will often play a role. In particular, the classical prediction that

linear electrophoresis does not result in any relative motions is likely to prove wrong in many experiments, where velocity fluctuations and hydrodynamic diffusion are likely to arise as a result of DIP. While this study focused on ideally polarizable particles, such as metallic colloids for instance, many microfluidic applications use dielectric particles which are only weakly polarizable. In this case, the expected qualitative difference will be the relative importance of DEP and ICEP: ICEP was previously shown to become much weaker in this case (Dukhin 1986; Squires & Bazant 2004; Yossifon *et al.* 2007), so that interactions overall will also be weaker, and particle chaining may still arise as a result of DEP, depending on the type of particles used.

The authors gratefully acknowledge discussions with Dr Klint Rose, and funding from Lawrence Livermore National Laboratory under subcontract DOE-B583843.

Supplementary movies are available at journals.cambridge.org/flm.

REFERENCES

Abramowitz, M. & Stegun, I. A. 1965 *Handbook of Mathematical Functions: With Formulas, Graphs, and Mathematical Tables*. Dover.

Abu Hamed, M. & Yariv, E. 2009 Boundary-induced electrophoresis of uncharged conducting particles: near-contact approximation. *Proc. R. Soc.* A **465**, 1939–1948.

Acrivos, A., Jeffrey, D. J. & Saville, D. A. 1990 Particle migration in suspensions by thermocapillary or electrophoretic motion. *J. Fluid Mech.* **212**, 95–110.

Anderson, J. L. 1985 Droplet interactions in thermocapillary motion. *Intl J. Multiph. Flow* **11**, 813–824.

Bazant, M. Z. & Squires, T. M. 2004 Induced-charge electrokinetic phenomena: theory and microfluidic applications. *Phys. Rev. Lett.* **92**, 066101.

Bazant, M. Z. & Squires, T. M. 2010 Induced-charge electrokinetic phenomena. *Current Opin. Colloid Interface Sci.* **15**, 203–213.

Bergougnoux, L. & Guazzelli, E. 2009 Non-Poisson statistics of settling spheres. *Phys. Fluids* **21**, 091701.

Butler, J. E. & Shaqfeh, E. S. G. 2002 Dynamic simulations of the inhomogeneous sedimentation of rigid fibres. *J. Fluid Mech.* **468**, 205–237.

Chen, S. B. & Keh, H. J. 1988 Electrophoresis in a dilute dispersion of colloidal spheres. *AIChE J.* **34**, 1075–1085.

Deserno, M. & Holm, C. 1997 How to mesh up Ewald sums. Part I. A theoretical and numerical comparison of various particle mesh routines. *J. Chem. Phys.* **109**, 7678–7693.

Drazer, G., Koplik, J., Khusid, B. & Acrivos, A. 2002 Deterministic and stochastic behaviour of non-Brownian spheres in sheared suspensions *J. Fluid Mech.* **460**, 307–335.

Dukhin, A. S. 1986 Pair interaction of particles in electric field. Part 3. Hydrodynamic interaction of ideally polarizable metal particles and dead biological cells. *Colloid J. USSR* **48**, 376–381.

Dukhin, A. S. & Murtsovkin, V. A. 1986 Pair interaction of particles in electric field. Part 2. Influence of polarization of double layer of dielectric particles on their hydrodynamic interaction in a stationary electric field. *Colloid J. USSR* **48**, 203–209.

Essmann, U., Perera, L., Berkowitz, M. L., Darden, T., Lee, H. & Pedersen, L. G. 1995 A smooth particle mesh Ewald method. *J. Chem. Phys.* **103**, 8577–8593.

Füredi, A. A. & Valentine, R. C. 1962 Factors involved in the orientation of microscopic particles in suspensions influenced by radio frequency fields. *Biochim. Biophys. Acta* **56**, 33–42.

Gamayunov, N. I., Murtsovkin, V. A. & Dukhin, A. S. 1986 Pair interaction of particles in electric field. Part I. Features of hydrodynamic interaction of polarized particles. *Colloid J. USSR* **48**, 197–203.

Ham, J. M. & Homsy, G. M. 1988 Hindered settling and hydrodynamic dispersion in quiescent sedimenting suspensions. *Intl J. Multiph. Flow* **14**, 533–546.

Happel, J. & Brenner, H. 1965 *Low Reynolds Number Hydrodynamics*. Prentice-Hall.

Hasimoto, H. 1959 On the periodic fundamental solutions of the Stokes equations and their application to viscous flow past a cubic array of spheres. *J. Fluid Mech.* **5**, 317–328.

Henry, D. C. 1931 The cataphoresis of suspended particles. Part I. The equation of cataphoresis. *Proc. R. Soc. Lond.* A **133**, 106–129.

Hiemenz, P. C. & Rajagopalan, R. 1997 *Principles of Colloid and Surface Chemistry*. CRC.

Hoffman, B. D. & Shaqfeh, E. S. G. 2009 The effect of Brownian motion on the stability of sedimenting suspensions of polarizable rods in an electric field. *J. Fluid Mech.* **624**, 361–388.

Jeffrey, D. J. 1973 Conduction through a random suspension of spheres. *Proc. R. Soc. Lond. Ser.* A **335**, 355–367.

Jeffrey, D. J. & Onishi, Y. 1984 Calculation of the resistance and mobility functions for two unequal rigid spheres in low-Reynolds-number flow. *J. Fluid Mech.* **139**, 261–290.

Jones, T. B. 1995 *Electromechanics of Particles*. Cambridge University Press.

Kim, S. & Karrila, S. P. 1991 *Microhydrodynamics: Principles and Selected Applications*. Butterworth-Heinemann.

Lei, X., Ackerson, B. J., & Tong, P. 2001 Settling statistics of hard sphere particles. *Phys. Rev. Lett.* **86**, 3300–3303.

Miloh, T. 2008*a* Dipolophoresis of nanoparticles. *Phys. Fluids* **20**, 063303.

Miloh, T. 2008*b* A unified theory of dipolophoresis for nanoparticles. *Phys. Fluids* **20**, 107105.

Miloh, T. 2009 Nonlinear alternating electric field dipolophoresis of spherical nanoparticles. *Phys. Fluids* **21**, 072002.

Morrison, F. A. 1970 Electrophoresis of a particle of arbitrary shape. *J. Colloid Interface Sci.* **34**, 210–214.

Murtsovkin, V. A. 1996 Nonlinear flows near polarized disperse particles. *Colloid J. USSR* **58**, 341–349.

Nott, P. R. & Brady, J. F. 1994 Pressure-driven flow of suspensions: simulations and theory. *J. Fluid Mech.* **275**, 157–199.

Patankar, N. A. 2009 Are the hydrodynamic forces and torques zero during electrophoresis of multiparticle systems with thin Debye layers? *Mech. Res. Commun.* **36**, 39–45.

Pine, D. J., Gollub, J. P., Brady, J. F. & Leshansky, A. M. 2005 Chaos and threshold for irreversibility in sheared suspensions. *Nature* **438**, 997–1000.

Pohl, H. A. 1978 *Dielectrophoresis*. Cambridge University Press.

Pozrikidis, C. 1992 *Boundary Integral and Singularity Methods for Linearized Viscous Flow*. Cambridge University Press.

Reed, L. D. & Morrison, F. A. 1975 Hydrodynamic interactions in electrophoresis. *J. Colloid Interface Sci.* **54**, 117–133.

Rose, K. A., Meier, J. A., Dougherty, G. M. & Santiago, J. G. 2007 Rotational electrophoresis of striped metallic microrods. *Phys. Rev.* E **75**, 011503.

Rose, K. A., Hoffman, B., Saintillan, D., Shaqfeh, E. S. G. & Santiago, J. G. 2009 Hydrodynamic interactions in metal rodlike-particle suspensions due to induced charge electro-osmosis. *Phys. Rev.* E **79**, 011402.

Russel, W. B., Saville, D. A. & Schowalter, W. R. 1989 *Colloidal Dispersions*. Cambridge University Press.

Saintillan, D. 2008 Nonlinear interactions in electrophoresis of ideally polarizable particles. *Phys. Fluids* **20**, 067104.

Saintillan, D., Darve, E. & Shaqfeh, E. S. G. 2005 A smooth particle-mesh Ewald algorithm for Stokes suspension simulations: the sedimentation of fibers. *Phys. Fluids* **17**, 033301.

Saintillan, D., Darve, E. & Shaqfeh, E. S. G. 2006*a* Hydrodynamic interactions in the induced-charge electrophoresis of colloidal rod dispersions. *J. Fluid Mech.* **563**, 223–259.

Saintillan, D., Shaqfeh, E. S. G. & Darve, E. 2006*b* Stabilization of a suspension of sedimenting rods by induced-charge electrophoresis. *Phys. Fluids* **18**, 121701.

Shilov, V. N. & Simonova, T. S. 1981 Polarization of electric-double-layer of dispersive particles and dipolophoresis in steady (DC) field. *Colloid J. USSR* **43**, 90–96.

Sierou, A. & Brady, J. F. 2001 Accelerated Stokesian dynamics simulations. *J. Fluid Mech.* **448**, 115–146.

Simonov, I. N. & Dukhin, A. S. 1973 Theory of electrophoresis of solid conducting particles in case of ideal polarization of a thin diffuse double layer. *Colloid J. USSR* **35**, 173–176.

Simonova, T. S., Shilov, V. N. & Shramko, O. A. 2001 Low-frequency dielectrophoresis and the polarization interaction of uncharged spherical particles with an induced Debye atmosphere of arbitrary thickness. *Colloid J.* **63**, 108–115.

Smoluchowski, M. 1903 Contribution à la théorie de l'endosmose électrique et de quelques phénomènes corrélatifs. *Bull. Intl Acad. Sci. Cracovie* **8**, 182–200.

Squires, T. M. 2009 Induced-charge electro-kinetics: fundamental challenges and opportunities. *Lab on a Chip* **9**, 2477–2483.

Squires, T. M. & Bazant, M. Z. 2004 Induced-charge electro-osmosis. *J. Fluid Mech.* **509**, 217–252.

Squires, T. M. & Bazant, M. Z. 2006 Breaking symmetries in induced-charge electro-osmosis and electrophoresis. *J. Fluid Mech.* **560**, 65–101.

Squires, T. M. & Quake, S. R. 2005 Microfluidics: fluid physics at the nanoliter scale. *Rev. Mod. Phys.* **77**, 977–1026.

Viovy, J. L. 2000 Electrophoresis of DNA and other polyelectrolytes: physical mechanisms. *Rev. Mod. Phys.* **72**, 813–872.

Wang, X., Wang, X.-B. & Gascoyne, P. R. C. 1997 General expressions for dielectrophoretic force and electrorotational torque derived using the Maxwell stress tensor method. *J. Electrostat.* **39**, 277–295.

Yariv, E. 2005 Induced-charge electrophoresis of nonspherical particles. *Phys. Fluids* **17**, 051702.

Yariv, E. 2009 Boundary-induced electrophoresis of uncharged conducting particles: remote wall approximations. *Proc. R. Soc.* A **465**, 709–723.

Yossifon, G., Frankel, I. & Miloh, T. 2007 Symmetry breaking in induced-charge electro-osmosis over polarizable spheroids. *Phys. Fluids* **19**, 068105.

Zhao, H. & Bau, H. H. 2007 On the effect of induced electro-osmosis on a cylindrical particle next to a surface. *Langmuir* **23**, 4053–4063.

Zinchenko, A. Z. 1994 An efficient algorithm for calculating multiparticle thermal interaction in a concentrated dispersion of spheres. *J. Comput. Phys.* **111**, 120–135.